PHYSICAL REVIEW APPLIED **7,** 044010 (2017)

Robust and Stable Delay Interferometers with Application to d-Dimensional Time-Frequency Quantum Key Distribution

Nurul T. Islam,[1,*] Clinton Cahall,[2] Andrés Aragoneses,[1,3] A. Lezama,[1,4] Jungsang Kim,[2] and Daniel J. Gauthier[5]
[1]*Department of Physics and the Fitzpatrick Institute for Photonics, Duke University, Durham, North Carolina 27708, USA*
[2]*Department of Electrical Engineering and the Fitzpatrick Institute for Photonics, Duke University, Durham, North Carolina 27708, USA*
[3]*Department of Physics and Astronomy, Carleton College, Northfield, Minnesota 55057, USA*
[4]*Instituto de Física, Universidad de la República. Casilla de correo 30, 11000 Montevideo, Uruguay*
[5]*Department of Physics, The Ohio State University, 191 West Woodruff Avenue, Columbus, Ohio 43210 USA*

(Received 16 November 2016; revised manuscript received 21 February 2017; published 18 April 2017)

We experimentally investigate a cascade of temperature-compensated unequal-path interferometers that can be used to measure frequency states in a high-dimensional quantum distribution system. In particular, we demonstrate that commercially available interferometers have sufficient environmental isolation so that they maintain an interference visibility greater than 98.5% at a wavelength of 1550 nm over extended periods with only moderate passive control of the interferometer temperature ($< \pm 0.50\,^{\circ}\mathrm{C}$). Specifically, we characterize two interferometers that have matched delays: one with a free spectral range of 2.5 GHz and the other with 1.25 GHz. We find that the relative path of these interferometers drifts less than 3 nm over a period of 1 h during which the temperature fluctuates by $< \pm 0.10\,^{\circ}\mathrm{C}$. When we purposely heat the interferometers over a temperature range of 20–50 °C, we measure a path-length shift of 26 ± 9 nm/°C for the 2.5-GHz interferometer. For the 1.25-GHz interferometer, the path-length shift is nonlinear and is locally equal to zero at a temperature of 37.1 °C and is 50 ± 17 nm/°C at 22 °C. With these devices, we realize a proof-of-concept quantum key distribution experiment and achieve quantum bit error rates of 1.94% and 3.69% in time and frequency basis, respectively, at a quantum channel loss of 14 dB.

DOI: 10.1103/PhysRevApplied.7.044010

I. INTRODUCTION

Quantum key distribution (QKD) allows two authenticated parties, Alice and Bob, to share a random key that is secured using the fundamental properties of quantum mechanics [1]. The field has progressed rapidly in the last two decades, where most practical QKD protocols encode information in two-dimensional (qubit) states of a photon, such as polarization or relative phase. Today, state-of-the-art QKD systems can generate a finite-length secure key at a rate of megabits per second [2–4] and at distances over 300 km [5,6], albeit at lower rates.

Despite the significant progress in realistic implementations, the key generation rates in qubit-based protocols are constrained by experimental nonidealities, such as the rate at which the quantum photonic states can be prepared or the dead time of single-photon-counting detectors. Moreover, in long-distance QKD, a large fraction of the information-carrying photons is lost in the quantum channel due to absorption or scattering. Such physical and practical limitations inspire new QKD protocols that can outperform qubit-based protocols in both secure key rate and distance.

A class of protocols that is predicted to provide better key rates with higher tolerance against errors involves encoding information in qudit states of photons [7–10]. We denote the dimension of the Hilbert space describing the quantum states by d, where $d = 2$ indicates a qubit and $d > 2$ indicates qudits. In high-dimensional schemes, information is encoded in various degrees of freedom of the photon, such as polarization, time frequency [11–18], spatial profiles [19–23], or a combination of these [24]. High-dimensional protocols have two primary advantages over qubit protocols. First, they allow multiple bits of information to be encoded on a single photon, hence, increasing the channel capacity. For some high-dimensional protocols, high photon efficiency can increase the secret key rate for high-loss channels, whereas others can improve the rate when the system is limited by detector saturation. Second, high-dimensional protocols are more robust to channel noise [7,8,25] and can tolerate a higher quantum bit error, thus, achieving secure communication at longer distances than qubit protocols [10].

We consider a high-dimensional time-bin encoding protocol where information is encoded in frames of time bins, and the presence of an eavesdropper is monitored by transmitting mutually-unbiased-basis (MUB) states with

---

[*] nti3@duke.edu

© 2017 American Physical Society

respect to time. For high-dimensional time-bin states, one choice for a MUB is to use states that are the discrete Fourier transform of the temporal states within a frame known as frequency or phase states [11].

The primary challenge of implementing this high-dimensional protocol is measuring the frequency states. One proposed method for measuring frequency states is to use a cascade of $d - 1$ unequal-path (time-delay) interferometers [11]. Experimentally, stabilizing the path difference in the interferometers to subwavelength-distance scales over long periods of time is challenging due to environmental disturbances such as temperature, pressure, and vibration, especially for large path differences. While active stabilization of the interferometers is possible, it greatly increases the system complexity.

An alternative approach is to use passively stabilized interferometers, which have been developed over the last decade by the optical telecommunication industry for use in classical phase- and frequency-domain protocols [26,27]. One design principle for addressing the thermal change of the path length is to adopt athermal design, where materials with different thermal expansion coefficients are used to achieve temperature compensation [28–30]. Furthermore, the sensitivity to pressure is reduced by hermetically sealing the interferometer, and the vibration sensitivity is reduced using a compact package.

Recently, other high-dimensional time-frequency QKD protocols based on continuous [12] or discrete variables [13] have been proposed using different approaches for measuring the frequency states based on dispersive optics, for example. The idea of these protocols is to create frequency states using a dispersive media such as a fiber Bragg grating that chirps a single-photon wave packet, which is decoded by Bob using a conjugate-dispersion-fiber Bragg grating followed by single-photon detectors, sometimes combined with a delay interferometer. However, matching the dispersion of the Bragg gratings at the transmitter and receiver in the presence of environmental disturbances is also challenging.

The primary purpose of this paper is to characterize the stability of commercially available, passively stabilized, unequal-path-length interferometers and assess their feasibility for detecting high-dimensional quantum photonic frequency states. By using these athermal interferometers, it is possible to eliminate the need for an active relative phase stabilization of Alice and Bob's interferometers often accomplished by sending strong coherent states between them [31,32], thus, eliminating possible Trojan-horse attacks by an eavesdropper [9,33]. In addition, these interferometers may find application in coherent one-way and differential-phase-shift QKD protocols [34–36] or in checking for coherence across many pulses as required for the round-robin protocols [37–39]. Finally, our setup can also be used to show a violation of Bell's inequality in high-dimensional systems [40,41].

The paper is organized as follows. In Sec. II, we give a brief description of two- and four-dimensional time-frequency QKD protocols and discuss how frequency states can be measured with a cascade of interferometers. In Sec. III, we discuss the basic design and stability (Sec. IV) of these interferometers. In Sec. V, we demonstrate a proof-of-principle QKD experiment, and we summarize our work and discuss potential future applications in Sec. VI.

II. TIME-FREQUENCY QKD PROTOCOL

We consider the two-basis time-frequency protocol proposed in Ref. [11], which is based on an entangled single-photon source, where Alice and Bob share a pair of hyperentangled photons [42]. For simplicity, the discussion below is restricted to the equivalent prepare-and-measure scenario, where Alice prepares and sends single-photon states and Bob measures the incoming states in one of two MUBs. In this protocol, time is discretized into bins of width τ and grouped into frames of d-contiguous time bins. A temporal state $|\Psi_{t_n}\rangle$ is created when the photonic wave packet is prepared in a single time bin within a frame, which encodes $\log_2 d$ bits. For the frequency states $|\Psi_{f_n}\rangle$, the photonic wave packet has an equal-height peak in every time bin within the frame, and each wave packet has a distinct relative phase. Here, the integrated probability over a frame is held constant for all of the time and frequency states. Figure 1 illustrates the $d = 2$ and $d = 4$ states.

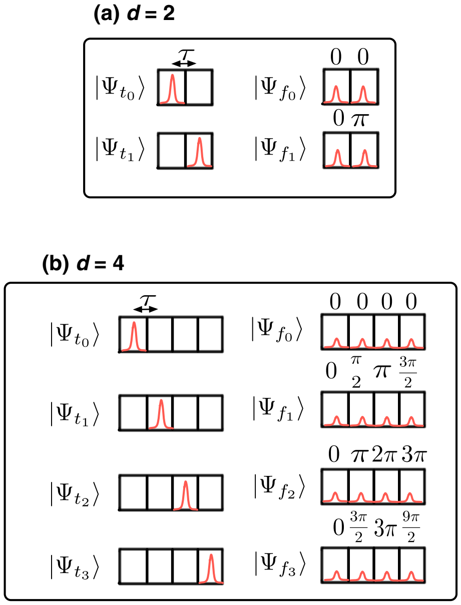

FIG. 1. Illustration of temporal (left) and frequency (right) states in terms of the wave-packet temporal positions for (a) $d = 2$ and (b) $d = 4$. The wave-packet peak shapes within each time bin represent the probability density of the photonic wave packet. The relative phase of the wave packets for the frequency states is labeled above each time bin.

In greater detail, the temporal states can be written as $|\Psi_{t_n}\rangle = a_n^\dagger|0\rangle$, where $a_n^\dagger$ is the field creation operator acting on a vacuum state in the nth temporal mode. Consequently, the frequency states can be written as [8]

$$|\Psi_{f_n}\rangle = \frac{1}{\sqrt{d}}\sum_{m=0}^{d-1}\exp\left(\frac{2\pi inm}{d}\right)|\Psi_{t_m}\rangle, \quad n=0,\ldots,d-1, \quad (1)$$

which is a natural extension of the BB84 temporal qubit states to higher dimension.

In a typical experimental implementation of a discrete-variable time-frequency QKD system, an attenuated laser is used to generate the photonic wave packets with a mean photon number of the order of 1, and a generalized decoy state protocol is used to put tight bounds on the fraction of wave packets that have more than one photon [4,43]. The temporal states can be generated by on or off encoding of a continuous-wave laser with a high-contrast intensity modulator. They can be measured directly with a single-photon detector with a jitter much less than τ and the event recorded with a high-resolution time tagger. The frequency states can be generated using a combination of phase and intensity modulators or with a cascade of delay interferometers considered here.

One scheme for measuring the frequency states is shown in Fig. 2(a) for the case $d = 2$, where we assume that the wave-packet peaks have a width much less than τ. Here, the relative phase difference is 0 for $|\Psi_{f_0}\rangle$ or π for $|\Psi_{f_1}\rangle$. As is apparent below, an empty "guard" prevents overlap of wave-packet peaks from neighboring frames when operating the QKD system at a high rate. A detailed analysis (not presented here) shows that this overlap does not affect the quantum bit error rate, and, hence, the guard bins are not necessarily needed. For clarity, we include the use of the guard bins in the discussion below.

In a time-delay interferometer, an incoming beam is split equally by a 50:50 beam splitter and directed along two different paths and recombined at a second 50:50 beam splitter where the wave packets interfere. The difference in the path between the two arms of the interferometer is denoted by $\Delta L = \Delta L_0 + \delta L$, where ΔL_0 is the nominal path difference. Here, $\delta L \ll \Delta L_0$ is a small path difference that allows us to make a fine adjustment to the transmission resonances of the interferometer and is proportional to the phase $\phi = k\delta L$, where k is the magnitude of the wave vector of the wave packet.

For $d = 2$, only a single time-delay interferometer is required with $\Delta L = c\tau$ corresponding to a free spectral range (FSR) $c/\Delta L$, where c is the speed of light, and ϕ is set to zero. When the state $|\Psi_{f_0}\rangle$ is incident on the interferometer, the wave packet traveling along the long path is delayed by τ with respect to the wave packet traveling along the short arm. After the second beam splitter, the wave packet originally occupying two time bins now occupies three (and, hence, explains the need for a guard bin), where only the wave-packet peak at the center of each frame interferes constructively (destructively) for the + (−) port. The earliest and the latest wave-packet peaks of the state do not interfere at the second beam splitter and, hence, do not directly give information about the frequency state. The situation is reversed when the state $|\Psi_{f_1}\rangle$ is incident on the interferometer (not shown).

For $d = 4$, one possible approach for measuring the frequency states uses a cascade of three time-delay interferometers as shown in the lower panel of Fig. 2(a). The first interferometer has a path difference of $2c\tau$, while the two interferometers connected to the output ports of

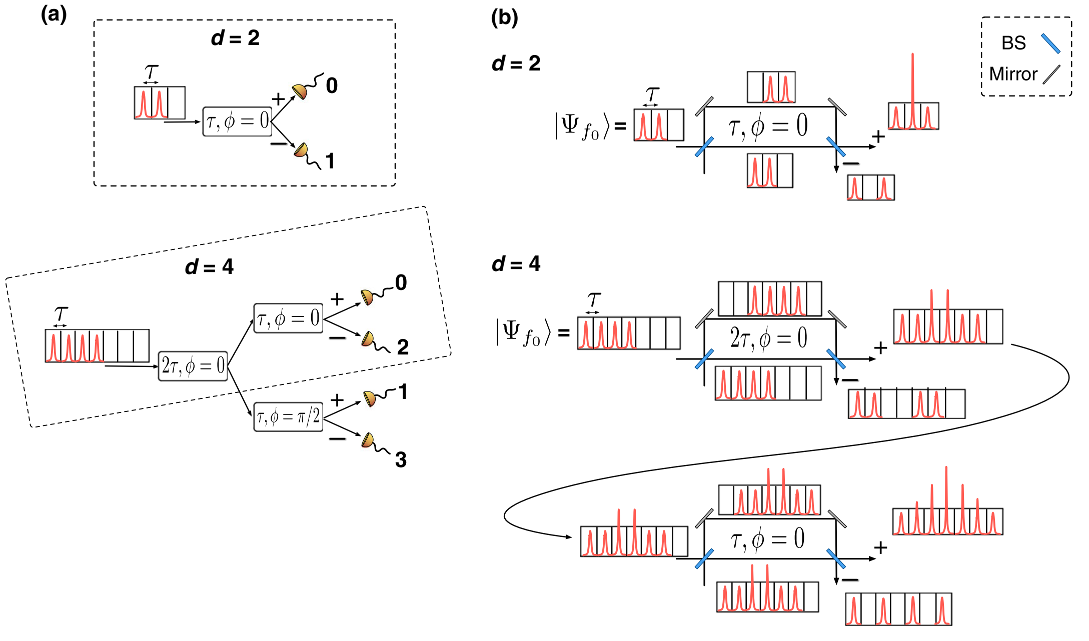

FIG. 2. (a) Schematic illustration of the frequency-state measurement technique for $d = 2$ (top panels) and $d = 4$ (bottom panels). (b) Frequency-state waveforms at different locations in the interferometers.

the first interferometer have a path difference of $c\tau$. The phase of the interferometer connected to the $+$ $(-)$ port of the first interferometer is set to $\phi = 0(\pi/2)$ whose outputs allow us to measure the frequency states $|\Psi_{f_0}\rangle$ and $|\Psi_{f_2}\rangle$ ($|\Psi_{f_1}\rangle$ and $|\Psi_{f_3}\rangle$).

The frequency states for $d = 4$ have four contiguous time bins occupied by wave-packet peaks of different relative phases and require three guard bins. When the state $|\Psi_{f_0}\rangle$ is incident on the first interferometer, as illustrated in Fig. 2(b), the wave packets are shifted temporally by 2τ when they arrive at the second beam splitter, and there is constructive (destructive) interference for the wave packets in the two middle time bins at the $+$ $(-)$ port of the interferometer. The two outer wave packets do not experience interference. These two sequences of wave packets are directed to the second set of interferometers of the next layer in the cascade. For simplicity, we describe only the interferences that take place in the interferometer with $\phi = 0$ indicated by the dashed box shown in the lower panel of Fig. 2(a).

At the $+$ $(-)$ output port of the second interferometer [lower panel of Fig. 2(b)], all seven time bins are occupied with the highest (lowest) probability for photon occupation for the time bin in the middle of the frame, which is due to constructive (destructive) interference of all four wave-packet peaks of the incident state. The other occupied time bins give information about interference of a subset of the incident wave-packet peaks except for the outermost time bins where no interference occurs. Thus, it is advantageous to measure all of the central five time bins because they each measure different aspects of the coherence of the incident wave-packet peaks. Because of the possibility of measuring the coherence among different sets of wave-packet peaks, the cascade of interferometers might also find use in the recently developed round-robin QKD protocol [39].

A similar analysis shows that the central time bin of each of the four outputs from the interferometer cascade are directly related to each of the frequency states. That is, constructive interference occurs in output port n when the state $|\Psi_{f_n}\rangle$ is incident on the cascade, and destructive interference is observed in the other three ports. The procedure for arbitrary d is given in Ref. [11] for which $2d - 1$ guard bins are required.

We note that the interferometric technique is only $1/d$ efficient in detecting the frequency states, which means that when considering the finite-key-length effects, $d > 4$ might not lead to a higher key rate. However, this intrinsic loss can be overcome by transmitting a large number of signals, where the asymptotic secret key length can be approached. Therefore, the interferometric technique for $d > 4$ is likely to give an incremental gain in the ultimate secure key rate in a QKD system, also coming at the cost of increased experimental complexity.

In a time-frequency QKD protocol, the contrast (visibility) of the interference provides an estimate of the error introduced by an adversary (Eve) in the quantum channel. The visibility for a frequency state $|\Psi_{f_n}\rangle$ is defined as

$$\mathcal{V} = \frac{\mathcal{P}_+ - \mathcal{P}_-}{\mathcal{P}_+ + \mathcal{P}_-}, \tag{2}$$

where $\mathcal{P}_+$ is the probability of detecting the photon in the expected bright port n in the central time bin, and $\mathcal{P}_-$ is the probability of finding the photon in any of the other ports in the same central time bin. The interference visibility is limited in a real device by the accuracy of the beam-splitting ratio, differential loss in the paths, and larger beam diffraction in one path in comparison to the other. Eve's interaction with the quantum states results in a loss of temporal coherence of the frequency states and, thus, results in a reduction of $\mathcal{V}$. A security analysis determines the maximum error rate that can be tolerated and, hence, the minimum value of $\mathcal{V}$.

III. TIME-DELAY INTERFEROMETERS

The delay-line interferometers used in the experiment are manufactured by Kylia and are of the Mach-Zehnder type but use a folded design reminiscent of a Michelson interferometer with displaced input and output beams [28,29] to make the design more compact and simpler (Fig. 3). Here, the incoming beam of light is split into two unequal paths using a 50∶50 beam splitter, displaced by the dihedral reflectors, recombined at the same beam splitter, and directed to two output ports. The overall phase ϕ of the interferometer is adjusted by changing the optical path of one arm of the interferometer relative to the other using a resistive heater placed near one of the reflectors. The path change is proportional to the power delivered to the resistor; applying ≤3 V results in a path-length change of approximately one FSR. Our devices are designed to operate over the classical optical telecommunication C band, and we evaluate their performance at 1550 nm near the middle of the band.

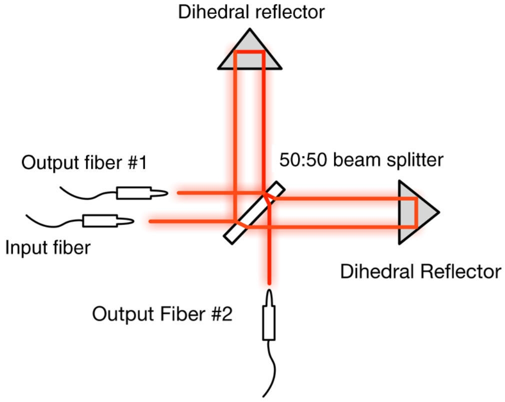

FIG. 3. Illustration of the internal components of a typical delay-line interferometer [44].

The stability of these interferometers against environmental changes depends on the thermal compensation method. While the Kylia design is proprietary, typical temperature-compensated delay-line interferometers use materials with a low coefficient of thermal expansion and an optimized selection of glasses and air paths for thermal and chromatic compensation [28–30]. The Kylia devices are realized using ultra-low-expansion optical glass components and base plate and packaged inside a hermetically sealed aluminum housing, which stabilizes them against environmental temperature and pressure, respectively.

IV. INTERFEROMETER PERFORMANCE

The change in path of the interferometer δL as a function of temperature T is typically specified by a temperature-dependent path-length shift (TDPS), but the time scale over which this characteristic is measured is usually not specified, and the use of only a single metric assumes that it is independent of T. As we show here, such a simple metric is not sufficient to adequately describe the relation between δL and the change in temperature ΔT. This is due to the fact that the outer package is made from aluminum, the internal interferometer is constructed from potentially different types of glass, and the input and output fibers must pass through the outer aluminum package. These materials have vastly different thermal conductivities and heat capacities, and the detailed design of the thermal link between them is proprietary. As we describe below, we observe two different time scales for the TDPS and that it can be a nonlinear function of T, indicating that the standard commercial specification is insufficient.

We investigate the performance of two Kylia delay-line interferometers, one with a FSR of 1.25 GHz ($\Delta L_0 = 24$ cm, $\tau = 800$ ps) and the other with 2.5 GHz ($\Delta L_0 = 12$ cm, $\tau = 400$ ps). The performance of these devices is characterized by observing the variation in the power of light emerging from one of the output ports when a continuous-wave, single-frequency laser beam is injected into the interferometer, as shown in Fig. 4(a), for three situations: (1) long-term (approximately 1 h) stability in a controlled laboratory environment (temperature control of ± 0.1 °C), (2) long-term (approximately 1 h) visibility in the same laboratory environment, and (3) the TDPS as we vary T between 20 and 50 °C.

Based on the specification of the interferometers (TDPS < 50% of the FSR over a 0–70 °C temperature range), we expect the shift in resonance frequency of the interferometers to be less than 10 MHz for $T < 0.5$ °C, which is typical in a laboratory environment. In order to measure such a small variation, we use a frequency-stabilized laser (Wavelength Reference Clarity NLL-1550-HP locked to a hydrogen cyanide molecular absorption line and operating in the "line-narrowing" mode) with an absolute accuracy of $\leq \pm 0.3$ pm and a specified long-term root-mean-square frequency stability better than 1 MHz.

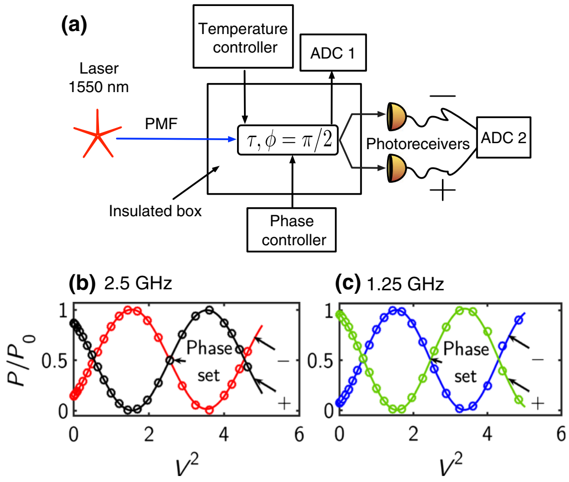

FIG. 4. (a) Schematic of the setup used to evaluate the performance of the interferometers. A 200-μW continuous-wave laser beam is injected into the interferometer using a polarization-maintaining fiber (PMF). The temperature of the interferometer is monitored using multiple thermocouples placed at different locations on the interferometers and digitized using ADC 1 (National Instruments NI-9239). The output powers are recorded using two photoreceivers (New Focus 2011) and digitized using ADC 2 (National Instruments NI-9239). The power at the two outputs of the (b) 2.5-GHz and (c) 1.25-GHz interferometers as a function of the square of the voltage applied to the resistive heater.

For all measurements, the interferometers are placed in a thermally insulated box and allowed to equilibrate for approximately 2 h with a mean initial temperature of 21.3 ± 0.3 °C. For the stability and TDPS measurements at a nominally constant T, the phase of the interferometer is set at the beginning of the equilibration process to the steepest slope of the interference fringe ($\phi = \pi/2$), as shown in Fig. 4(b). If $\phi \neq \pi/2$ at the end of the equilibration process, a small change is made to bring it back to this point. For the visibility measurement, ϕ is set to zero to place it at an interference maximum. For the TDPS measurements over a wider range, T is set between 20 and 50 °C using heating tapes wrapped around the device, which are connected to a variable voltage supply.

A. Stability at nominally constant temperature

The optical power emerging from the $\pm$ ports of an ideal (high-visibility) time-delay interferometer is given by

$$P_{\mathrm{out},\pm} = \frac{\alpha P_0}{2}[1 \pm \cos(k\Delta L)], \tag{3}$$

where P_0 is the power at the input of the interferometer, and the parameter $\alpha \in \{0, 1\}$ represents the reduced transmission due to insertion loss of the interferometer. We find that the predominant contribution to the variation in $P_{\text{out},\pm}$ arises from imperfect thermal compensation and hermetic sealing of the device, giving rise to a change in δL. The power at the output is given by

$$\begin{aligned}\frac{2P_{\text{out},\pm}}{\alpha P_0} &= \{1 \pm \cos[k(\Delta L_0 + \delta L)]\} \\ &= [1 \pm \cos(\phi \pm k\delta L)], \qquad (4) \\ &= [1 \mp \sin(k\delta L)], \qquad (5)\end{aligned}$$

where we insert the phase $\phi \equiv k\Delta L_0 = \pi/2$ between Eqs. (4) and (5). Equation (5) relates the output power of the interferometer initially set at $\phi = \pi/2$ to δL assuming a stable laser frequency, and we use it to estimate the drift of the interferometer.

The emitted power can also change due to other physical effects, which cause us to incorrectly associate a change δL with a change in $P_{\text{out},\pm}$. We use various methods to account for this systematic error in our measurement. To account for variation in the incident laser power P_0 (typically below 0.01%), we place a 50:50 fiber beam splitter just before the interferometer with one output defining the reference laser power $P_r(t)$, while the other output is directed to the interferometer. The ratio between the peak power emitted by one output of the interferometer and the reference power is given by α.

For the stability measurements, we find that both the 1.25- and 2.5-GHz interferometers display an apparent drift of less than 3 nm over 1 h if the temperature of the environment is stabilized to ±0.1 °C as it is in the cardboard enclosure. Figure 5(a) shows one such measurement of δL [extracted from the data using Eq. (5)] for the 2.5-GHz interferometer, with the corresponding change in temperature in Fig. 5(b). We observe that δL is not fully correlated with ΔT (0.8 correlation coefficient). The lack of stronger correlation can be attributed to two additional factors that affect the apparent drift of the interferometer.

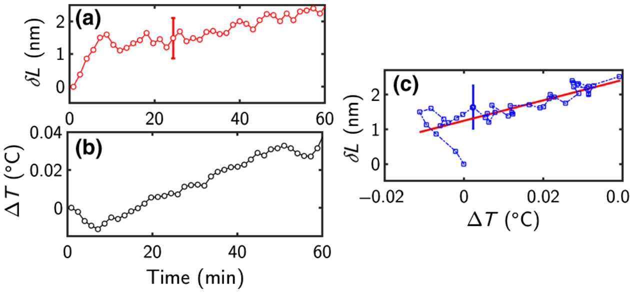

FIG. 5. (a) The path-length drift of the 2.5-GHz interferometer measured over 1 h. (b) The corresponding temperature variation monitored over the same period of time. (c) The path-length drift from (a) plotted as a function of the temperature variation from (b).

First, there is a contribution to the drift of the interferometer due to laser-frequency fluctuation. We expect the drift of the frequency-stabilized laser to be better than 1 MHz over 1 h, which corresponds to an apparent path-length change of 0.62 nm for the 2.5-GHz interferometer as indicated by the error bars in Figs. 5(a) and 5(c). To estimate the contribution of laser drift to this data set, we fit it to a linear function as indicated by the red line. We attribute the finite slope of the line as arising from the change in the path of the interferometer, which is 1.2 ± 0.1 nm. This slope is likely an upper bound to the actual path-length change given that it is within the range of the specified laser-frequency drift.

From these data, we also determine the root-mean-square error (RMSE) between the data and the fit. The measured RMSE of 0.32 nm corresponds to a possible laser-frequency variation of 0.51 MHz, well within the specified deviation of <1 MHz, and, thus, we attribute these smaller-scale fluctuations in the data to the laser-frequency drift. Clearly, it is evident that the laser-frequency variation is a significant contribution to the apparent path-length change of the interferometer.

A second factor that can give rise to an imperfect correlation between δL and ΔT is the fact that we measure T of the aluminum outer package, which may not reflect the actual temperature of the substrate and optics housed inside the aluminum package (see discussion below). The effect of such a lag on these data is difficult to determine from measurements over such a small temperature change. To address this issue, we conduct a set of measurements for a larger temperature range in Sec. IV C below.

To ensure that the laser variation plays a dominant role in these measurements, in Fig. 6 we show similar plots for the 1.25-GHz interferometer, but we choose a particular set of data where the temperature change of the device (approximately 0.01 °C) is much less than for the 2.5-GHz interferometer. In Fig. 6(a), we observe that the interferometer apparently drifts substantially in the first

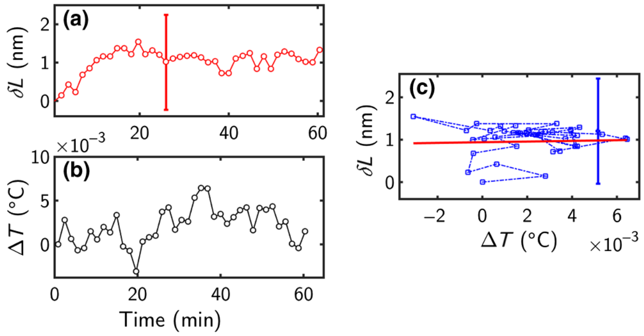

FIG. 6. (a) The path-length drift of the 1.25-GHz interferometer for three independent runs measured over 1 h. (b) The corresponding temperature variation monitored over the same period of time. (c) The path-length drift from (a) plotted as a function of the temperature variation from (b).

approximately 20 min of the run and then stabilizes to within approximately 1.2 nm thereafter. Again, there is little correlation between δL and ΔT (-0.03 correlation coefficient). Following a similar procedure that we describe above, we find that a straight-line fit to the data shown in Fig. 6(c) has a slope of zero, implying no path-length change over this temperature range. Furthermore, the RMSE between the linear fit and the data corresponds to a path difference of 0.34 nm and can be attributed to a 0.27-MHz drift in the laser frequency, well within the specification of the laser. We note that the 1-MHz specification of the laser frequency now translates to a 1.24-nm change in path length as indicated by the error bars in Fig. 6(b) and 6(c).

We perform a similar analysis on several independent data sets collected for both the interferometers and observe similar stability. Specifically, we observe that $\delta L < 3$ nm over 1 h if the interferometers are stabilized to $<0.1\,^{\circ}\mathrm{C}$. This measurement is an upper bound to the true path-length change because the variation of the frequency of the stabilized laser gives rise to a comparable apparent shift.

B. Visibility

As we discuss in the text related to Eq. (2) above, the interferometer visibility $\mathcal{V}$ is a critical QKD system parameter used to determine an upper bound on the effects due to an eavesdropper. Thus, to extract the largest possible key, it is important to characterize the base-line change in $\mathcal{V}$ due to environmental conditions, which sets a lower limit on the error due to Eve that can be detected. To this end, we inject a continuous-wave, frequency-stabilized laser beam into the interferometer [see Fig. 4(a)], set $\phi = 0$, and monitor the power coming out of the output ports, denoted by $P_{\max}$ at the $+$ output port and $P_{\min}$ at the $-$ output port. We then determine $\mathcal{V}$ using Eq. (2), where the probabilities $\mathcal{P}_+$ and $\mathcal{P}_-$ are replaced with powers $P_{\max}$ and $P_{\min}$. We do not monitor the laser power in these measurements because the typical variations in laser power ($<0.01\%$) have less than a 0.004% effect on $\mathcal{V}$.

Figure 7 shows the temporal behavior of $\mathcal{V}$ and ΔT for both interferometers measured independently at two different times, each over the course of 1 h. We note that the temperature changes are slightly larger ($<\pm 0.5\,^{\circ}\mathrm{C}$) than for the stability measurement that we discuss in the previous section. For both interferometers, we find that the visibilities stay well over 98.5% during the entire hour. The error bars indicate the expected change in $\mathcal{V}$ for a typical drift in the laser frequency of 1 MHz. This error is determined by propagating uncertainties and the covariance of the dependent variables $P_{\max}$ and $P_{\min}$.

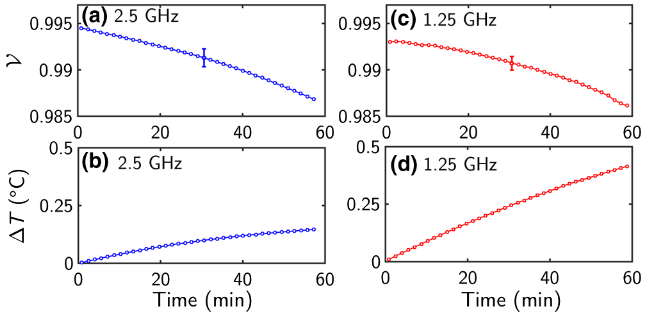

FIG. 7. (a),(c) The visibility of the 2.5- and 1.25-GHz interferometers measured over 1 h, respectively. (b),(d) The temperature variation of the 2.5- and 1.25-GHz interferometers measured over 1 h, respectively.

One potentially useful application of the delay interferometers is to perform frequency-state measurements for a wavelength-division-multiplexed time-frequency QKD system. To assess the Kylia devices for this application, we use a widely tunable laser (Agilent HP81862A) to measure $\mathcal{V}$ for both interferometers between 1525 and 1565 nm (approximately over the entire C band) in approximately 5-nm steps. We find that $\mathcal{V} > 99\%$ across this range. This is consistent with Kylia's specification of $>98.4\%$ over the wavelength range of 1520–1570 nm. Thus, in a wavelength-multiplexed system, a single set of interferometers can be used for the frequency measurement for each wavelength channel, and a wavelength demultiplexer can be placed after the interferometers to send each channel to their respective detectors. Therefore, a high-data-throughput time-frequency QKD system can be realized without using a separate delay-interferometer cascade for each spectral channel.

C. Wide-range temperature-dependent path-length shift

To obtain a better estimate of the TDPS that is not as sensitive to the laser-frequency fluctuations, we measure δL over a wider temperature range, where the path-length shift is expected to be larger. The setup is identical to that described in Sec. IV above, except that we purposefully vary the device temperature in large steps. We collect data at each temperature step for at least 6 h. After this interval, we heat the device again to a new temperature, repeating this procedure until the total temperature change is approximately $30\,^{\circ}\mathrm{C}$ from an initial temperature of approximately $22\,^{\circ}\mathrm{C}$.

Figure 8 shows the variation in δL with T for the 2.5-GHz interferometer over four heating intervals (intervals indicated by vertical dashed lines). At the beginning of each interval, we observe that the temperature of the aluminum housing increases and then levels off. We find that the data are well described by a single-exponential function with a rate constant of $1.28 \pm 0.01\ \mathrm{h}^{-1}$ averaged over the four time intervals [Fig. 8(b)]. The data and the fit are overlaid in the figure and are indistinguishable (reduced $\chi^2 = 1.34$). From Fig. 8(a), we see that there is a correspondingly rapid increase in δL, followed by a slower continued rise. We find that the data are fit well by a double exponential with two

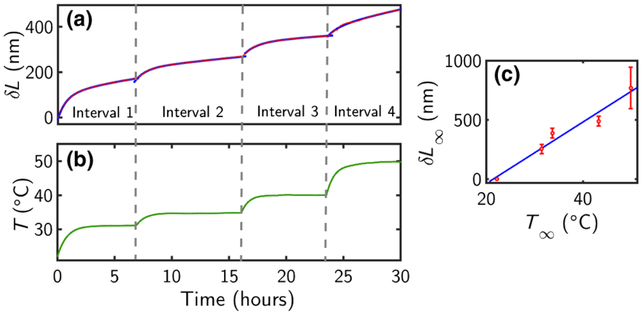

FIG. 8. Temperature-dependent path-length shift for the 2.5-GHz interferometer. (a) Variation in the path change as the interferometer is heated in four intervals. The rate constants for the double-exponential fit for intervals 1–4 are $(1.4 \pm 0.1, 0.10 \pm 0.04)$, $(1.3 \pm 0.1, 0.10 \pm 0.02)$, $(1.3 \pm 0.1, 0.23 \pm 0.04)$, and $(1.6 \pm 0.6, 0.07 \pm 0.06)$ h^{-1}, respectively, and the long-time extrapolated path changes δL_∞ are 253 ± 80, 135 ± 3, 101 ± 19, and 280 ± 170 nm, respectively. (b) Variation in the temperature as the interferometer is heated. The rate constants for the exponential fit for intervals 1–4 are 1.223 ± 0.007, 1.370 ± 0.007, 1.48 ± 0.02, and 1.047 ± 0.005 h^{-1}, respectively, and the extrapolated temperatures are 32.35 ± 0.03, 36.1 ± 0.2, 41.6 ± 0.1, and 50.78 ± 0.03 °C, respectively. (c) Temperature dependence of the long-time extrapolated path change along with a fit to a straight line.

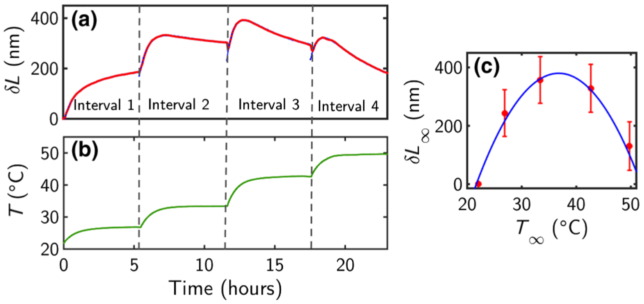

FIG. 9. Temperature-dependent path-length shift for the 1.25-GHz interferometer. (a) Variation in the path change as the interferometer is heated in four intervals. The rate constants for the double-exponential fit for intervals 1–4 are $(1.4 \pm 0.2, 0.2 \pm 0.1)$, $(1.2 \pm 0.2, 0.6 \pm 0.2)$, $(1.9 \pm 0.1, 0.28 \pm 0.04)$, and $(1.8 \pm 0.1, 0.24 \pm 0.02)$ h^{-1}, respectively, and the long-time extrapolated path changes δL_∞ are 244 ± 80, 114 ± 3, -50 ± 10, and -198 ± 12 nm, respectively. (b) Variation in the temperature as the interferometer is heated. The rate constants for the exponential fit for intervals 1–4 are 1.101 ± 0.002, 1.330 ± 0.001, 1.277 ± 0.003, and 1.48 ± 0.01 h^{-1}, respectively and the extrapolated temperatures are 27.89 ± 0.01, 34.69 ± 0.01, 43.90 ± 0.08, 50.94 ± 0.04 °C, respectively. (c) Temperature dependence of the long-time extrapolated path change along with a fit to a quadratic function.

different rate constants; the fit function is again overlaid with the measurements and is nearly indistinguishable (reduced $\chi^2 = 1.42$). The two average rate constants are 1.4 ± 0.2 and 0.13 ± 0.02 h^{-1}. The larger rate constant is similar to that for the rise in T, and we attribute this change in path due to coupling between the aluminum housing and the interferometer, likely due to mechanical coupling between the two. The lower heat conductivity of the interferometer glass likely contributes to making the other rate constant so long.

To estimate the total change in δL for each interval, even though we do not collect data long enough to reach equilibrium, we use our double-exponential fit to find the long-time limit for the path change, which we denote by δL_∞, and the single-exponential fit to find T_∞. We note that this fitting technique is only an estimate because it assumes a change in δL that is linear with temperature after a sufficiently long settling time. Figure 8(c) shows δL_∞ as a function of T_∞, which we fit with a straight line. From this fit, we find that the TDPS is 26 ± 9 nm/°C. The TDPS specified by Kylia is 11 nm/°C, which is clearly smaller than what we estimate for our device. This could be due to imperfect temperature compensation for this device.

We observe similar behavior for the 1.25-GHz interferometer as shown in Fig. 9. Importantly, we observe that the contribution to δL from the glass can counteract that due to the aluminum housing for the last three intervals. Using the same fitting procedure as above, we find that the average rate constant for the temperature change is 1.297 ± 0.003 h^{-1}, and the two rate constants for the path change are 1.57 ± 0.08 and 0.33 ± 0.06 h^{-1}. Again, there is a strong correlation between the temperature rate constant and the fast rate constant for the path change, indicating that the aluminum housing plays an important role in our observations. Using our fit to extrapolate to long times for each interval, we find that the path change is a nonlinear function of T (well fit by a quadratic in this case), and, hence, a single value for the TDPS does not adequately characterize this device. Just considering the data point for the first interval, the inferred TDPS is 50 ± 17 nm/°C, which again exceeds the specification of 22 nm/°C. However, the TDPS is zero at 37.1 °C based on our fit to a quadratic.

V. PROOF-OF-CONCEPT QKD EXPERIMENT

To demonstrate the applicability of these interferometers in a high-dimensional ($d = 4$) time-frequency QKD protocol, we implement a proof-of-principle experiment using the setup as shown in Fig. 10.

We create temporal and frequency states by modulating the amplitude and phase of a continuous-wave laser. Specifically, a pulse train of 66-ps-width wave packets is created from a continuous-wave laser beam using a Mach-Zehnder modulator and a 5-GHz sine-wave generator. A second Mach-Zehnder modulator driven with an arbitrary serial pattern generator produced by a 10-GHz transceiver located on a field-programmable gate array (FPGA) is used to select the wave packets within a 1.6-ns-long temporal frame. The time-bin width is set to 400 ps, matched to the

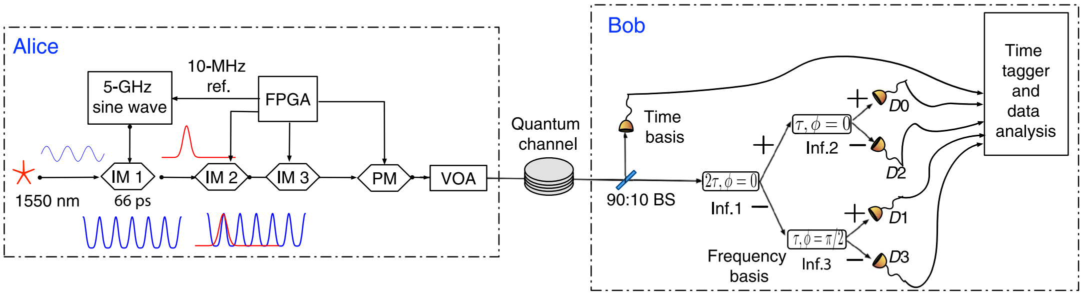

FIG. 10. Schematic illustrating the experimental details for the proof-of-principle demonstration. A 1550-nm continuous-wave laser (Agilent HP81862A, power 1 mW) is modulated into a pulse train of 66-ps-width wave packets using a Mach-Zehnder modulator (EOSPACE). The optical modulator driver (JDSU H301) used as an amplifier at the input of the modulator is driven with a 5-GHz sine-wave generator. The field-programmable gate array (Stratix V FPGA 5SGXEA7N2F40C2N, Terasic Stratix V Signal Integrity Kit) is used to create the temporal and frequency states with biased probabilities of 0.9 and 0.1, respectively. The frequency states are suppressed using a third Mach-Zehnder modulator to reduce the amplitude to one-fourth. A phase modulator is used to impose phases on the frequency states. At Bob's receiver, the incoming quantum states are directed to temporal- and frequency-basis-measurement devices using a 90:10 coupler. The output of the detectors are time tagged using a time-to-digital converter (Agilent U1051A Acquiris).

time delay τ of the second-stage interferometers (2.5-GHz FSR) in the interferometric setup. The FPGA is programmed to transmit a fixed pattern with 90% temporal and 10% frequency states at a repetition rate of 625 MHz. To have an equal probability of observing photons in either a temporal or a frequency state, we use a third intensity modulator, also driven by the FPGA, to lower the transmission during a frequency-state frame by a factor of 4. Three additional signals from the FPGA are combined to drive a phase modulator, which induces the appropriate phase for each peak making up the frequency state. The light is then attenuated using a variable optical attenuator to a mean photon number of approximately 0.5 photons per state. The single-photon wave packets are transmitted through a second variable optical attenuator to simulate losses in the quantum channel. For this measurement, we fix the attenuation in the quantum channel to 14 dB, equivalent to a standard fiber length of 70 km (0.2 dB/km). The average observed detection rate at this loss is 5.88×10^6.

When the single photons arrive at Bob's receiver, the wave packets are split using a beam splitter that directs 90% (10%) of the signal to the temporal (frequency) measurement devices. The incoming single photons in the temporal channel are measured using five identical high-efficiency (>70%), low-jitter (50 ps), fast-switching (>15-MHz detection rates) superconducting nanowire detectors with identical readout circuits. The frequency-basis measurement is performed using three delay interferometers in a tree structure, two with a FSR of 2.5 GHz and the other with a FSR of 1.25 GHz, and four single-photon detectors. For both temporal and frequency measurements, the detector outputs are time tagged using a 50-ps-resolution time-to-digital converter.

The performance of the QKD system is characterized by several key parameters, such as the error rates, the quality of the state preparation and detection, etc., all of which affect the secret key rate of an eventual full QKD system. Below, we present some key parameters of our prototype system.

A. MUB quality

We characterize the quality of the MUB states by calculating the overlap of the temporal- and frequency-basis states, $|\langle\Psi_{f_n}|\Psi_{t_m}\rangle|^2$, $\{m, n\} \in \{0, 1, 2, 3\}$. Specifically, we calculate the probability of detections when an input state is measured in both the basis in which it is created as well as in the other basis. Ideally, if an input state is measured in the basis in which it is created, the overlap is 1. Similarly, a state prepared in one basis and measured in an orthogonal basis has an equal probability of detection across all orthogonal modes. That is, states prepared and measured in orthogonal bases result in a uniformly random outcome, $|\langle\Psi_{f_n}|\Psi_{t_m}\rangle|^2 = 0.25$. This is illustrated in Fig. 11(a) where we assume that the state preparation and detection are perfect. The colored axis represents the probability of detections. The blocks along the diagonal represent the cases where an input state is measured in the same basis it is created, which results in an overlap of 1.

In Fig. 11(b), we plot the experimentally achieved overlap for all input states. The diagonal elements indicate a strong correlation between the prepared and measured states when the measured state coincides with the prepared state. The off-diagonal elements, especially when the states are prepared and measured in different bases, are very close to the ideal value of 0.25 as illustrated in Fig. 11(c), where we provide the values of the experimentally obtained matrix elements. When the frequency (temporal) states are measured in the temporal (frequency) basis, we calculate the standard deviation of the overlap to be 0.02 (0.006). Although the average overlap of our MUB states is close to ideal, a few of the matrix elements indicate that some of the states are not prepared or measured perfectly and will lead to quantum bit errors in our QKD system.

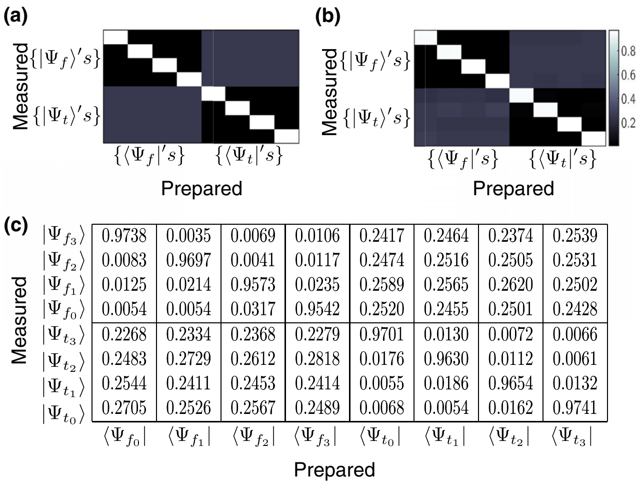

	$\langle\Psi_{f_0}|$	$\langle\Psi_{f_1}|$	$\langle\Psi_{f_2}|$	$\langle\Psi_{f_3}|$	$\langle\Psi_{t_0}|$	$\langle\Psi_{t_1}|$	$\langle\Psi_{t_2}|$	$\langle\Psi_{t_3}|$
$|\Psi_{f_3}\rangle$	0.9738	0.0035	0.0069	0.0106	0.2417	0.2464	0.2374	0.2539
$|\Psi_{f_2}\rangle$	0.0083	0.9697	0.0041	0.0117	0.2474	0.2516	0.2505	0.2531
$|\Psi_{f_1}\rangle$	0.0125	0.0214	0.9573	0.0235	0.2589	0.2565	0.2620	0.2502
$|\Psi_{f_0}\rangle$	0.0054	0.0054	0.0317	0.9542	0.2520	0.2455	0.2501	0.2428
$|\Psi_{t_3}\rangle$	0.2268	0.2334	0.2368	0.2279	0.9701	0.0130	0.0072	0.0066
$|\Psi_{t_2}\rangle$	0.2483	0.2729	0.2612	0.2818	0.0176	0.9630	0.0112	0.0061
$|\Psi_{t_1}\rangle$	0.2544	0.2411	0.2453	0.2414	0.0055	0.0186	0.9654	0.0132
$|\Psi_{t_0}\rangle$	0.2705	0.2526	0.2567	0.2489	0.0068	0.0054	0.0162	0.9741

FIG. 11. (a) Probabilities of detecting a state when the state preparation and measurement device is assumed to be perfect. (b) Experimentally achieved probabilities of detection. (c) Overlap matrix elements for all input states is determined using 4.96×10^6 total events in the time and frequency bases.

B. Error rates and visibility

Quantum bit error rates are important system parameters, which, combined with the rate of state preparation and detection, determine the secret key generation rate. The error rates in both bases are affected by several factors, such as the system temporal jitter, leakage of light through the intensity modulator, detector noise, uncorrelated photons entering the quantum channel, optical misalignment, etc. In addition to these factors, the error rate in the frequency basis is also affected by the quality of state preparation and visibility of the interferometers.

In our experiment, the quantum bit error rates in the time and frequency bases are measured to be 1.94% and 3.69%, respectively. We note that the observed error rates here are different than in Fig. 11(c) because these two data sets were taken at two different times. In Fig. 12(a), we show timing histograms when each of the four temporal states is detected in the timing basis. The FWHM of the histograms is approximately 110 ps, much smaller than the 400-ps time-bin window, which indicates that the system jitter is not the primary source of error in our measurement. In fact, the main source of error in our QKD system is the leakage of light from the intensity modulator; we estimate that approximately 1% error can be attributed to the finite extinction ratio of the intensity modulators.

Figure 12(b) shows the histograms obtained when the frequency state $|\Psi_{f_0}\rangle$ passes through the interferometric setup and the photons are detected in detectors $D0$, $D2$, $D1$, $D3$ (top to bottom panels). The observed constructive (destructive) interference pattern is similar to the expected intensity pattern as shown in Fig. 2. In Fig. 13, we plot the visibility of all four frequency states as a function of time during which the data are collected. The visibility is determined using Eq. (2), where we subtract 1.94% of the events to correct for the affect of leakage, detector noise, etc., and to estimate the visibility solely due to the state preparation and measurement.

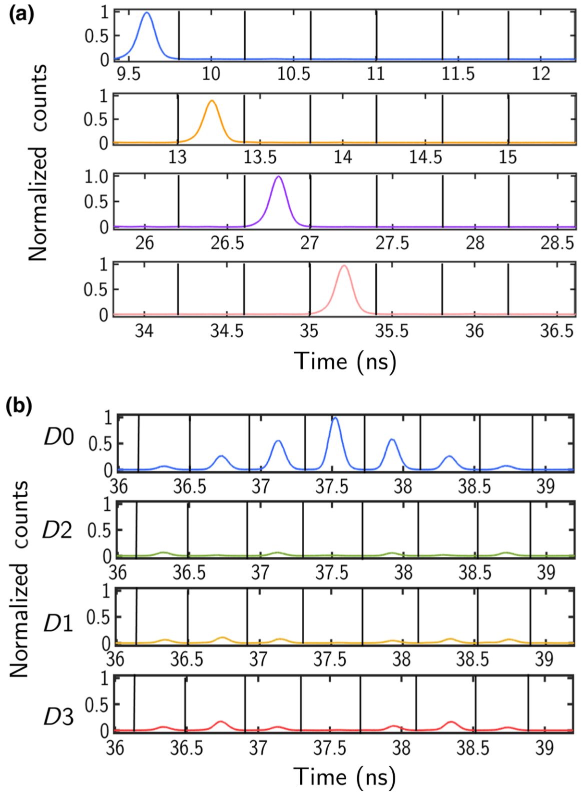

FIG. 12. (a) The timing histograms of temporal state $|\Psi_{t_0}\rangle$, $|\Psi_{t_1}\rangle$, $|\Psi_{t_2}\rangle$, and $|\Psi_{t_3}\rangle$ as measured during the experiment. (b) The timing histogram of frequency state $|\Psi_{f_0}\rangle$ measured at the output of the interferometric setup.

From Fig. 13, we observe that the visibility of the frequency state $|\Psi_{f_0}\rangle$ is >98% during the course of the data collection, similar to what we observe with classical light. On the other hand, the visibilities of $|\Psi_{f_1}\rangle$, $|\Psi_{f_2}\rangle$, and $|\Psi_{f_3}\rangle$ are smaller. We attribute the lower visibility of these states to imperfect state preparation.

In greater detail, the frequency states in our experiment are created by combining three amplified signals from the FPGA using a 3 : 1 coupler and using this signal to drive the

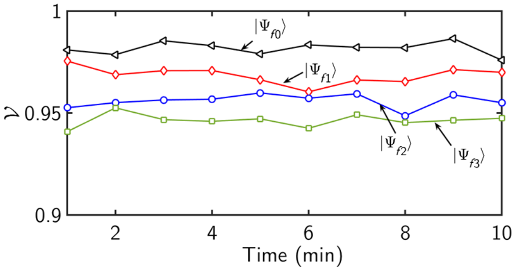

FIG. 13. Visibilities of all frequency states as a function of time.

phase modulator. There are two specific problems with this technique. First, the gain of each amplifier is slightly different and can cause deviation in phase from one time bin to another. Second, the timing of the combined signal needs to be matched to within tens of picoseconds, which is difficult given each path from the FPGA to the phase modulator is different. This nonideality can be corrected in future experiments using finely tunable digital delay lines and precision step attenuators.

VI. CONCLUSION

In conclusion, we demonstrate high environmental stability for commercially available temperature-compensated time-delay interferometers for application in discrete-variable time-frequency QKD. In particular, we observe that both the 2.5- and 1.25-GHz interferometers have a path-length stability of better than 3 nm when the temperature is maintained within $\pm 0.1\,^{\circ}\mathrm{C}$ in a laboratory environment. In addition, when heated in a controlled manner, we observe a TDPS of 26 ± 9 nm/°C for the 2.5-GHz device. For the 1.25-GHz interferometer, we observe a nonlinear change in path length as a function of the temperature, which is locally at zero at 37.1 °C and 50 ± 17 nm/°C at 22 °C. We argue that for such nonlinear devices, the TDPS metric is not sufficient. Rather, we have to assess both the stability at a constant temperature over a long time scale, as well as over a wide range of temperatures. We also investigate the possibility of using these passive interferometers as components in time-bin encoding QKD. We observe a maximum change of visibility of less than 1.0% over 1 h, which shows that if the temperature of these devices is maintained actively within $\pm 0.1\,^{\circ}\mathrm{C}$, then they can indeed be used for long-distance high-dimensional time-bin encoding QKD. We also demonstrate a proof-of-principle QKD experiment and achieve a quantum bit error rate of 1.94% (3.69%) in temporal (frequency) basis at a quantum channel loss of 14 dB. We conclude that these devices are suitable for realizing a high-dimension discrete-variable time-frequency QKD system.

ACKNOWLEDGMENTS

We gratefully acknowledge discussions of this work with Paul Kwiat, Charles Ci Wen Lim, William J. Brown, and Ludovic Fulop, and the financial support of the ONR MURI program on Wavelength-Agile Quantum Key Distribution in a Marine Environment, Grant No. N00014-13-1-0627.

[1] S. Barnett, *Quantum Information*, Oxford Master Series in Physics (Oxford University Press, Oxford, 2009).

[2] N. Walenta *et al.*, A fast and versatile quantum key distribution system with hardware key distillation and wavelength multiplexing, New J. Phys. **16**, 013047 (2014).

[3] M. Lucamarini, K. A. Patel, J. F. Dynes, B. Fröhlich, A. W. Sharpe, A. R. Dixon, Z. L. Yuan, R. V. Penty, and A. J. Shields, Efficient decoy-state quantum key distribution with quantified security, Opt. Express **21**, 24550 (2013).

[4] Charles Ci Wen Lim, Marcos Curty, Nino Walenta, Feihu Xu, and Hugo Zbinden, Concise security bounds for practical decoy-state quantum key distribution, Phys. Rev. A **89**, 022307 (2014).

[5] Boris Korzh, Charles Ci Wen Lim, Raphael Houlmann, Nicolas Gisin, Ming Jun Li, Daniel Nolan, Bruno Sanguinetti, Rob Thew, and Hugo Zbinden, Provably secure and practical quantum key distribution over 307 km of optical fibre, Nat. Photonics **9**, 163 (2015).

[6] Hua-Lei Yin, Teng-Yun Chen, Zong-Wen Yu, Hui Liu, Li-Xing You, Yi-Heng Zhou, Si-Jing Chen, Yingqiu Mao, Ming-Qi Huang, Wei-Jun Zhang, Hao Chen, Ming Jun Li, Daniel Nolan, Fei Zhou, Xiao Jiang, Zhen Wang, Qiang Zhang, Xiang-Bin Wang, and Jian-Wei Pan, Measurement-Device-Independent Quantum Key Distribution over a 404 km Optical Fiber, Phys. Rev. Lett. **117**, 190501 (2016).

[7] H. Bechmann-Pasquinucci and W. Tittel, Quantum cryptography using larger alphabets, Phys. Rev. A **61**, 062308 (2000).

[8] Nicolas J. Cerf, Mohamed Bourennane, Anders Karlsson, and Nicolas Gisin, Security of Quantum Key Distribution Using *d*-Level Systems, Phys. Rev. Lett. **88**, 127902 (2002).

[9] Valerio Scarani, Helle Bechmann-Pasquinucci, Nicolas J. Cerf, Miloslav Dušek, Norbert Lütkenhaus, and Momtchil Peev, The security of practical quantum key distribution, Rev. Mod. Phys. **81**, 1301 (2009).

[10] Lana Sheridan and Valerio Scarani, Security proof for quantum key distribution using qudit systems, Phys. Rev. A **82**, 030301 (2010).

[11] Thomas Brougham, Stephen M. Barnett, Kevin T. McCusker, Paul G. Kwiat, and Daniel J. Gauthier, Security of high-dimensional quantum key distribution protocols using Franson interferometers, J. Phys. B **46**, 104010 (2013).

[12] Jacob Mower, Zheshen Zhang, Pierre Desjardins, Catherine Lee, Jeffrey H. Shapiro, and Dirk Englund, High-dimensional quantum key distribution using dispersive optics, Phys. Rev. A **87**, 062322 (2013).

[13] J. Nunn, L. J. Wright, C. Söller, L. Zhang, I. A. Walmsley, and B. J. Smith, Large-alphabet time-frequency entangled quantum key distribution by means of time-to-frequency conversion, Opt. Express **21**, 15959 (2013).

[14] Zheshen Zhang, Jacob Mower, Dirk Englund, Franco N. C. Wong, and Jeffrey H. Shapiro, Unconditional Security of Time-Energy Entanglement Quantum Key Distribution Using Dual-Basis Interferometry, Phys. Rev. Lett. **112**, 120506 (2014).

[15] Daniel J. Gauthier, Christoph F. Wildfeuer, Hannah Guilbert, Mario Stipcevic, Bradley G. Christensen, Daniel Kumor, Paul Kwiat, Kevin T. McCusker, Thomas Brougham, and Stephen Barnett, *Quantum Information and Measurement* (Optical Society of America, Rochester, New York, 2013).

[16] Tian Zhong, Hongchao Zhou, Robert D. Horansky, Catherine Lee, Varun B. Verma, Adriana E. Lita, Alessandro Restelli, Joshua C. Bienfang, Richard P. Mirin, Thomas

Gerrits, Sae Woo Nam, Francesco Marsili, Matthew D. Shaw, Zheshen Zhang, Ligong Wang, Dirk Englund, Gregory W. Wornell, Jeffrey H. Shapiro, and Franco N. C. Wong, Photon-efficient quantum key distribution using time-energy entanglement with high-dimensional encoding, New J. Phys. **17**, 022002 (2015).

[17] Thomas Brougham, Christoph F. Wildfeuer, Stephen M. Barnett, and Daniel J. Gauthier, The information of high-dimensional time-bin encoded photons, arXiv:1506.04420.

[18] B. Brecht, Dileep V. Reddy, C. Silberhorn, and M. G. Raymer, Photon Temporal Modes: A Complete Framework for Quantum Information Science, Phys. Rev. X **5**, 041017 (2015).

[19] Mohammad Mirhosseini, Omar S. Magaa-Loaiza, Malcolm N. O'Sullivan, Brandon Rodenburg, Mehul Malik, Martin P. J. Lavery, Miles J. Padgett, Daniel J. Gauthier, and Robert W. Boyd, High-dimensional quantum cryptography with twisted light, New J. Phys. **17**, 033033 (2015).

[20] S. P. Walborn, D. S. Lemelle, M. P. Almeida, and P. H. Souto Ribeiro, Quantum Key Distribution with Higher-Order Alphabets Using Spatially Encoded Qudits, Phys. Rev. Lett. **96**, 090501 (2006).

[21] Sebastian Etcheverry, Gustavo Cañas, E. S. Gómez, W. A. T. Nogueira, C. Saavedra, G. B. Xavier, and Gustavo Lima, Quantum key distribution session with 16-dimensional photonic states, Sci. Rep. **3**, 2316 (2013).

[22] G. Caas, N. Vera, J. Carie, P. Gonzlez, J. Cardenas, P. W. R. Connolly, A. Przysiezna, E. S. Gmez, M. Figueroa, G. Vallone, P. Villoresi, T. Ferreira da Silva, G. B. Xavier, and G. Lima, High-dimensional decoy-state quantum key distribution over 0.3 km of multicore telecommunication optical fibers, arXiv:1610.01682.

[23] Yunhong Ding, Davide Bacco, Kjeld Dalgaard, Xinlun Cai, Xiaoqi Zhou, Karsten Rottwitt, and Leif Katsuo Oxenlwe, High-dimensional quantum key distribution based on multicore fiber using silicon photonic integrated circuits, arXiv:1610.01812.

[24] Julio T. Barreiro, Nathan K. Langford, Nicholas A. Peters, and Paul G. Kwiat, Generation of Hyperentangled Photon Pairs, Phys. Rev. Lett. **95**, 260501 (2005).

[25] Irfan Ali-Khan, Curtis J. Broadbent, and John C. Howell, Large-Alphabet Quantum Key Distribution Using Energy-Time Entangled Bipartite States, Phys. Rev. Lett. **98**, 060503 (2007).

[26] David Hillerkuss *et al.*, in *Proceedings of Optical Fiber Communication Conference* (Optical Society of America, San Diego, California, 2010).

[27] D. Hillerkuss, R. Schmogrow, T. Schellinger, M. Jordan, M. Winter, G. Huber, T. Vallaitis, R. Bonk, P. Kleinow, F. Frey *et al.*, 26 tbit $s-1$ line-rate super-channel transmission utilizing all-optical fast Fourier transform processing, Nat. Photonics **5**, 364 (2011).

[28] G. Thuillier and Gordon G. Shepherd, Fully compensated Michelson interferometer of fixed-path difference, Appl. Opt. **24**, 1599 (1985).

[29] William A. Gault, Sean F. Johnston, and David J. W. Kendall, Optimization of a field-widened Michelson interferometer, Appl. Opt. **24**, 1604 (1985).

[30] Y. C. Hsieh, Michelson interferometer based delay line interferometers, U. S. Patent No. 7,522,343 (21 April 2009).

[31] A. Muller, H. Zbinden, and N. Gisin, Quantum cryptography over 23 km in installed under-lake telecom fibre, Europhys. Lett. **33**, 335 (1996).

[32] G. Ribordy, J. D. Gautier, N. Gisin, O. Guinnard, and H. Zbinden, Automated plug & play, quantum key distribution, Electron. Lett. **34**, 2116 (1998).

[33] Nitin Jain, Elena Anisimova, Imran Khan, Vadim Makarov, Christoph Marquardt, and Gerd Leuchs, Trojan-horse attacks threaten the security of practical quantum cryptography, New J. Phys. **16**, 123030 (2014).

[34] Nicolas Gisin, Gregoire Ribordy, Hugo Zbinden, Damien Stucki, Nicolas Brunner, and Valerio Scarani, Towards practical and fast quantum cryptography, arXiv:quant-ph/0411022.

[35] Tobias Moroder, Marcos Curty, Charles Ci Wen Lim, Le Phuc Thinh, Hugo Zbinden, and Nicolas Gisin, Security of Distributed-Phase-Reference Quantum Key Distribution, Phys. Rev. Lett. **109**, 260501 (2012).

[36] Kyo Inoue, Edo Waks, and Yoshihisa Yamamoto, Differential Phase Shift Quantum Key Distribution, Phys. Rev. Lett. **89**, 037902 (2002).

[37] Toshihiko Sasaki, Yoshihisa Yamamoto, and Masato Koashi, Practical quantum key distribution protocol without monitoring signal disturbance, Nature (London) **509**, 475 (2014).

[38] Jian-Yu Guan, Zhu Cao, Yang Liu, Guo-Liang Shen-Tu, Jason S. Pelc, M. M. Fejer, Cheng-Zhi Peng, Xiongfeng Ma, Qiang Zhang, and Jian-Wei Pan, Experimental Passive Round-Robin Differential Phase-Shift Quantum Key Distribution, Phys. Rev. Lett. **114**, 180502 (2015).

[39] Hiroki Takesue, Toshihiko Sasaki, Kiyoshi Tamaki, and Masato Koashi, Experimental quantum key distribution without monitoring signal disturbance, Nat. Photonics **9**, 827 (2015).

[40] J. D. Franson, Bell Inequality for Position and Time, Phys. Rev. Lett. **62**, 2205 (1989).

[41] Adetunmise C. Dada, Jonathan Leach, Gerald S. Buller, Miles J. Padgett, and Erika Andersson, Experimental high-dimensional two-photon entanglement and violations of generalized Bell inequalities, Nat. Phys. **7**, 677 (2011).

[42] Julio T. Barreiro, Nathan K. Langford, Nicholas A. Peters, and Paul G. Kwiat, Generation of Hyperentangled Photon Pairs, Phys. Rev. Lett. **95**, 260501 (2005).

[43] Hoi-Kwong Lo, Xiongfeng Ma, and Kai Chen, Decoy State Quantum Key Distribution, Phys. Rev. Lett. **94**, 230504 (2005).

[44] Ludovic Fulop and Kylia (private communication).